



Machine learning-based fault diagnosis for research nuclear reactor medium voltage power cables in fraction Fourier domain

Mohamed H. Saad¹ · Abdelrahman Said²

Received: 27 May 2022 / Accepted: 7 September 2022 / Published online: 19 September 2022
© The Author(s) 2022

Abstract

Fault diagnosis of Medium Voltage power Cables (MVCs) research nuclear reactor, incredibly inaccessible/remote ones, has to be carefully identified, located, and fixed within a short time. Therefore, this paper proposes a perfect simultaneous fault diagnosis scheme based on Multiclass Support-Vector Machine (MCSVM) in the fractional Fourier domain. First, the three-phase sending currents are simulated under different conditions then their features are extracted using Discrete Fractional Fourier Transform (DFRFT). Afterward, the features reduction process occurs via the Singular Value Decomposition (SVD) approach. MCSVM scheme is used to diagnose faults (i.e., discover, categorize, and trace) using reduced features outcome from DFRFT and SVD stages. Alternating Transient Program/Electromagnetic Transient Program (ATP/EMTP) simulations have been carried out for 22 kV unreachable MVC. Different kernels of SVM, i.e., linear, quadratic, or polynomial, and diverse factors of DFRFT, i.e., α , are investigated in simulations to obtain the optimum performance (i.e., best α and kernel pair). Hence, performance analysis of the proposed diagnosis method under different conditions (i.e., various fault resistances, locations, and inception angles) concluded two highest accuracy and lowest time settings, which were found at $\alpha = 0.5$ (for both) quadratic kernel, and linear kernel, respectively. Moreover, the linear kernel achieves 99.8% accuracy rate, the lowest execution time (10 ms), and fault tracing error rate of 0.525789%, which is proper for real-time applications. Besides, our proposed method is more reliable and accurate against variable operating conditions (fault resistances, distances, and inception angles), leading to more reliable power production systems.

Keywords Fault diagnosis · ATP/EMTP · MCSVM · DFRFT · SVD · MVCs · Nuclear reactor

1 Introduction

Electric power plants, especially nuclear ones, are spread worldwide as a leading source of electricity for subscribers. Recently, underground power distribution networks have played a crucial role by integrating different power plants into distributed networks, changing the system's behavior and affecting the system [1, 2]. Typically, MVCs are buried underground rather than overhead to feed electric plants, preserving them against adversary weather conditions [3].

However, those cables might still malfunction with asymmetric and symmetric faults due to insulation breakdown or external damage [4]. Moreover, they are spread in urban areas, industries, nuclear, and densely populated areas. Since traditional fault diagnosis methods consume time and cost, the reliance on automated intelligent solutions increases. Hence, lately, real-time monitoring solutions for systems have recently received significant interest. Among cable fault tracing, in particular, has become crucial in industrial applications, owing to its primary role in interconnecting each electrical element [2].

Without precise fault prediction and tracing solutions for those MVCs research nuclear reactor, it can overload the electric network, resulting in hazardous transients, excessive heating, i.e., fire and explosion, equipment failure, power outages, and losing system reliability [5–7]. Over the years, there have been many different ways to measure the location of faults in transmission networks [8]. However, due

✉ Abdelrahman Said
abdelrahman.ghoniem@feng.bu.edu.eg

¹ Radiation Engineering Department, National Center for Radiation Research and Technology (NCRRT), Egyptian Atomic Energy Authority, Cairo, Egypt

² Department of Electrical Engineering, Faculty of Engineering at Shoubra, Benha University, Cairo 11672, Egypt

to structural differences between underground cables distribution networks and the transmission network, some of the current solutions are not proper for both power network types [8]. Efficient fault location necessitates the integration of knowledge and methods. It is required to complete the task rapidly in order to limit nuclear reactor outages and prevent future damage to the cable system. This comprises understanding of cable system design, construction, and proper fault locating processes, which should include a high resistance fault. Hence, this paper provides a precise fault tracing solution for MVCs in distributed networks feeding research nuclear reactor.

A well-known fault diagnosis methods including Machine Learning (ML) techniques [9], impedance-based methods [10], traveling wave-based algorithms [11], and state estimation-based approaches [12]. The authors of [6] surveyed different fault detection methods, including their pros and cons. The transient patterns of voltage and current are used to determine the fault distance in transient-based fault location methods [13]. Moreover, in [14], in comparison to prior impedance-based approaches, a fault location methodology was proposed that uses both the peak time and amplitude of the fault current at the local place with reasonable accuracy and speed. The authors of [15] discussed applying wavelets for locating faults in distribution systems, resulting in several milliseconds of fault detection speed. Still, such a method cannot trace faults.

Manual outage mapping utilizing information from customers is now the most prevalent method for predicting the fault location [16]. However, new fault location methods in distribution systems have been proposed as a result of recent improvements in monitoring systems. The location of the fault is identified using deep graph deep learning approach in [17]. The graph network model is utilized to locate the fault in this method, which uses input from various sensors on separate buses. [18] suggests installing phasor measurement units (PMU) in the distribution system to develop fault location identification. This method locates the defect using real-time data from PMUs and state estimation. However, it necessitates a high-bandwidth communication connection as well as additional costs for equipment installation. In actual systems, however, just the current and voltage at the upstream power substation are monitored. The fault location can be estimated by calculating the impedance between the problematic point and the substation [19]. In general, existing approaches estimate the fault location in these instances, where only the power substation is monitored, by ignoring fault resistance and load impact during the fault. The pattern recognition method was used to define the fault localization problem in [20] and [21], but it requires extensive databases, which include fault cases for the entire distribution system. As a result, in addition to reliable system modeling, there is

always the chance of differing findings when testing in realistic distribution systems. In [22], a traveling wave-based method for fault location in a radial distribution system is proposed. However, because of the large number of laterals in distribution systems, this method necessitates the use of additional equipment and has low accuracy in experimental conditions. [23] Proposes a method for locating faults in a medium voltage (MV) distribution system's underground cable using current and voltage sensors at the primary substation 10 kV feeder. The current and voltage waveforms measured by an overcurrent relay at the head end of the MV distribution system are used instead of installing additional sensor devices. The key transient features for estimating the fault are the peak time and current value. Previous related work concentrated only on a few forms of fault detection without tracing or fastly fixing the problem. Moreover, previous methods are inadequate and unreliable due to the over cost of sensors. The precision of the location in the traveling-wave-based approach, for example, is heavily dependent on the performance of the expensive high-speed data collecting system, and the fault location is identified by traveling wave timing analysis. The voltage and current during pre-fault and post-fault are acquired and analyzed in the impedance-measurement-based technique. The transmission line model can then be used to determine the line parameters, and the fault can be located. The earlier work was less accurate and effective in synchronous supervisor and decentralized control over the whole power cable. With this backdrop, we developed an exact approach based on MCSVM in fraction Fourier domain for fault identification and location of underground power cables feeding research nuclear reactors. Only delivering end transient current for fault detection and classification, this technology was considered a low-cost, high-precision solution.

Lately, SVM has witnessed remarkable achievements in many research areas, such as face recognition, signal processing, and fault diagnosis. Moreover, SVM-based classifiers have better generalization properties than artificial neural networks (ANN)-based classifiers as their efficiency do not depend on the number of features. Hence, such merit is beneficial in fault diagnostics due to the unlimited number of features in our case, making it possible to compute directly using original data without pre-processing them to extract their features. Therefore, SVM is an excellent choice for fault detection and localization applications. Moreover, it is applicable to any distribution system. However, we focus here on research nuclear reactor faults due to its severe importance and safety as it may cause national disaster.

The following are the main contributions of this paper: -

- A novel supervised machine learning-based fault diagnosis approach for MVC feeding research nuclear reactor

using Multiclass Support-Vector Machine (MCSVM) in fractional Fourier domain.

- The Alternating Transient Program/Electromagnetic Transient Program (ATP/EMTP) is used to simulate an actual 22 kV MVCs that are fed to our proposed method.
- First, Discrete Fractional Fourier Transform (DFRFT) extracts features from ATP/EMTP current signal. The DFRFT processes both spatial and frequency domains of the processed current signal. Therefore, it is appropriate to handle different fractional power parameters of the current signal throughout the spatial–frequency domain to enhance the classification performance.
- Singular Vector Decomposition (SVD) extracts the essential features by removing each phase’s most significant singular value. This feature reduction helps in reducing the classifier’s processing time, which is proper for real time.
- Afterward, MCSVM approach is used to detect, classify, and trace faults using the output current training patterns obtained from previous stages.
- The performance of our proposed method is studied against different fractional power parameters and various kernels of SVM to find out the near-optimal pair.
- In addition, the MCSVM performance is investigated under various fault conditions (fault resistances (R) and inception angles (Θ)).

Paper organization is as follows: Sect. 2 highlights the concepts of DFRFT, SVD, and MCSVM schemes. Section 3 describes the system model, namely, 22kv MVC, research nuclear reactor load, and faults. The proposed fault diagnosis algorithm for the system under study is discussed in Sect. 4. Section 5 shows ATP/EMTP simulated fault results followed by simulation results. Finally, Sect. 6 summarizes the paper.

2 FRFT, SVD, and SVM overview

This section will briefly discuss FRFT, SVD, and SVM schemes since they are utilized in our proposed fault diagnosis algorithm.

2.1 Fractional Fourier transform (FRFT)

The FRFT, proposed by N.Victor [24], generalizes the Fourier Transform (FT) used in various disciplines, including signal processing, quantum mechanics, quantum optics, optical systems, and communication systems. FT determines the spectral content of a signal, not the spectral components’ time location [24]. The FRFT algorithm rotates signals in the time–frequency domain. Time–frequency patterns are critical when analyzing time-varying or non-stationary signals. FRFT forms the signals as rotations in the time–frequency

plane as a powerful tool for signal analysis. In this case, an order parameter is utilized to introduce revolve in the time–frequency plane. As a result, the FRFT can convert a signal $x(t)$ to $X_\alpha(u)$, which is represented in an intermediate domain between time and frequency.

$$X_\alpha(u) = FRFT_\alpha(x(t)) = \int_{-\infty}^{\infty} x(t) \cdot K_\alpha(t, u) dt \tag{1}$$

where α is the transform order and K_α is the transform kernel that is calculated as follows:

$$K_\alpha = \begin{cases} \sqrt{\frac{1-j\cot(\alpha)}{2\pi}} e^{j\left(\frac{t^2}{2}\right)\cot(\alpha)} - jut\csc(\alpha) & \alpha \neq n\pi \\ \delta(t-u) & \alpha = 2n\pi \\ \delta(t+u) & \alpha = (2n \pm 1)\pi \end{cases} \tag{2}$$

The Dirac function is represented as $\delta(t)$. When α is equal to $\pi/2$, the FRFT transforms to the standard FT, i.e., the transformed signal is completely in the frequency domain. The converted signal, on the other hand, can be in the time domain if α is equal to 0. As a result, the FRFT has an extra degree of flexibility throughout the order parameter (α) compared to the FT.

Let $x(t)$ be a sampled periodic signal with a period Δ_0 . The α th order DFRFT of $x(t)$ can be mathematically expressed as follows [18]

$$f_\alpha = \sum_{K=-\frac{N}{2}}^{\frac{N}{2}-1} f\left(\frac{\Delta_0}{N}\right) \sum_{n=-\infty}^{\infty} K_\alpha\left(x\left(n + \frac{K}{N}\right)\Delta_0\right) \tag{3}$$

where N is the number of points and $k = 0,1,2,\dots,N$ of DFRFT matrix as diagonal elements. The coefficients of the DFRFT are determined by a fractional factor (α) ranging from 0 to 1 [25]. Thus, due to its superior benefits, we employ eigenvector DFRFT as a feature extractor in the proposed method (with a factor between 0 and 1).

2.2 Singular value decomposition (SVD)

SVD is an orthogonal transformation that simplifies the matrix into a diagonal form, whose eigenvalues reflect several of the original matrix’s primary characteristics. Specifically, it is a matrix factorization technique that is extremely useful for various tasks such as pattern recognition, data dimension reduction, matrix approximation, pseudo inverse calculation, and solving linear equations. SVD has been successfully applied to signal processing as a data processing method and approved its effectiveness at avoiding modal aliasing. It decomposes any singular matrix into upper, diagonal, and

lower matrices as follows:

$$A = U \cdot S \cdot V' \quad (4)$$

where U and V are unitary matrices, i.e., $UU' = 1$ and $VV' = 1$, called left and right singular vectors, respectively. The S matrix is a diagonal matrix representing the singular values of A , which are evaluated by calculating the eigenvalues of AA' . It can be described as follows:

$$S = \begin{pmatrix} s_1 & & & 0 \\ & \ddots & & \\ & & s_\rho & \\ & & & 0 \\ 0 & & & & \ddots \\ & & & & & 0 \end{pmatrix} \quad (5)$$

where ρ is the rank of the matrix A . Note that $s_1 > s_2 > \dots > s_\rho$, i.e., s_1 is the largest singular value. SVD extracts the unique features matrix in several values (singular values), so it is endowed with a dimension reduction strategy with good stability performance. In other words, when the feature matrix element changes, the single values do not vary significantly.

2.3 Support-vector machine (SVM)

SVM is a ML-based approach mainly utilized for classification and regression prediction [26], where it is used to maximize forecast accuracy while avoiding overfitting the data automatically. A system that uses the hypothesis space of a linear function in a high-dimensional feature space can be defined as this technique. This system is trained using an optimization-based learning algorithm that incorporates a learning bias derived from statistical learning theory. The SVM's primary objective is to find the optimal separating hyperplane that maximizes the training data's margin [27].

The optimal separating hyperplane is obtained by maximizing the margin between two or more training data set classes. The separable case's optimization problem (no misclassified training example)

$$\begin{aligned} \text{Minimize : } & \frac{1}{2} \|W\|^2 \\ \text{subject to the constrains : } & y_i (W \cdot C_i + b) \geq 1 \end{aligned} \quad (6)$$

where n denotes the number of training data points. Then, the solution to this problem is achieved by optimizing the following equation:

$$E = \frac{1}{2} \|W\|^2 - \sum_i \alpha_i \left(y_i \left(\vec{W} \cdot \vec{V}_i + b \right) - 1 \right) \quad (7)$$

where W is a collection of weights, one for each input feature, y is the output result that shows the class label ($y \in \{1, -1\}$ for binary classifier), and C is the input feature vectors V 's (also known as support vectors) are picked locations from the input training features' data (C) that satisfy the maximum margin above and below the hyperplane. The parameters b and α are used to determine a unique maximum margin solution. The chosen support vectors V 's are represented by the y 's and α 's. The decision function $d(Q)$, which is positive for class 1 and negative for class 2, predicts the classification of an unknown vector Q and is defined for kernel (K) as follows:

$$d(Q) = \text{sign} \left(\sum_i K(Q, V_i) \right) y_i \alpha_i + b \quad (8)$$

To classify the DFRFT transform's output, different SVM kernels such as the linear-SVM and nonlinear formulations such as the quadratic and Gaussian radial basis function (RBF) were investigated.

2.3.1 Multiclass SVM

SVM was developed to address the problem of binary classification. Numerous extensions to multiclass classification are proposed [28], including One-Versus-All (OVA), one-versus-one (OVO), and the Crammer–Singer multiclass extension. OVO-SVM generates all possible pairwise SVMs with training examples drawn from a set of N classes. For each pair of classes I and j , the decision function is defined as follows:

$$f^{ij}(x) = \left\langle \varphi(x) \cdot w^{ij} \right\rangle + b^{ij} \quad (9)$$

Different decision functions are used for $N(N-1)/2$ -class problems. Various strategies can be used to obtain a shared decision between the generated classifiers. The most common is majority voting, also referred to as "max-wins." Thus, the decision function can be defined as follows:

$$\arg \max_i \sum_{j \neq i, j=1}^k \text{sign}(f^{ij}(x)) \quad (10)$$

3 System model

3.1 MVC research nuclear reactor description

Figure 1 shows the layout of 22 kV MVC feeding research nuclear reactor have length 20 km, transmitted power is 1500 MVA, $0.024 + j0.23$ positive sequence and $0.412 + j1.13$ zero sequence impedance per phase in Ω [3, 23, 29]. A balanced direct-sequence three-phase set of 50 Hz sinusoidal currents

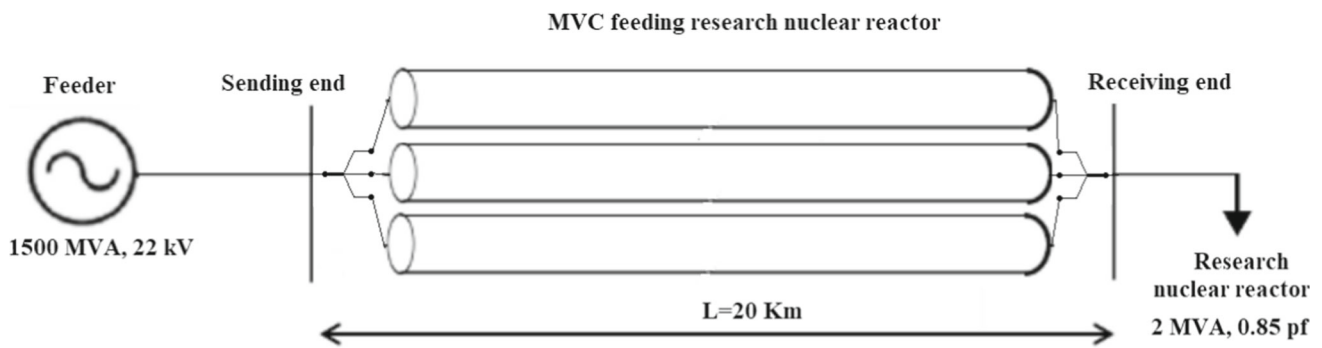
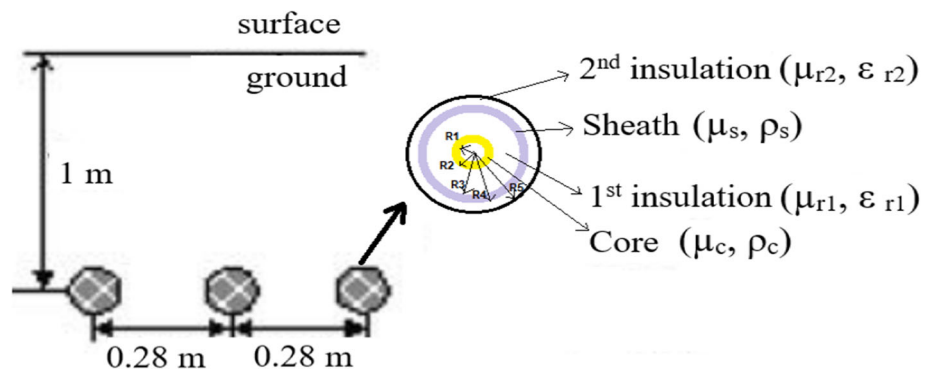


Fig. 1 Power network comprised of a research nuclear reactor load, a 20-km three-phase single-core MVC

Fig. 2 Structure and installation of the three-phase single core cable



specified by Eq. (11), with 53-A rms and 18 kV rms, defines the phase conductor currents and voltages.

$$I_p = 53 \left[1, e^{-j2\pi/3}, e^{j2\pi/3} \right] A \tag{11}$$

Due to significant influence on the nuclear underground cable behavior under different faults must be either accurately measured or reliably predicted by simulations. This performance requires accurate modeling of system components. As a result, high-frequency model components using ATP/EMTP are used to implement 22 kV MVC feeding research nuclear reactor load.

3.2 Power station modeling

The power station’s synchronous generator (SG = 1500 MVA/22 kV) is represented by the ATP/EMTP model SM59/58 have 14Ω resistance and 0.35 mH inductance.

3.3 MVC modeling

Figure 2 shows the underground cable type and geometry used in this study. Under identification of dimension of 22 kV underground cable as in Table 1, the MVC was simulated using the LCC JMarti model (Frequency-dependent model with constant transformation matrix), which was likewise based on traveling wave theory [3, 29, 30].

Table 1 Specification of 22 kV cross-linked polyethylene (XLPE) underground cable material

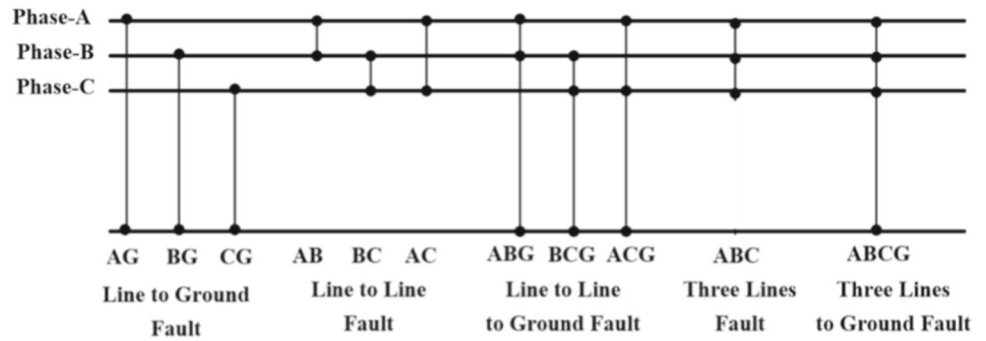
Radius (mm)	$R_1 = 0 \text{ mm}, R_2 = 20 \text{ mm}, R_3 = 40 \text{ mm}, R_4 = 43 \text{ mm}, R_5 = 45 \text{ mm},$
Core conductor	$\mu_c = 1, \rho_c = 1.724e^{-8} \Omega.m$
Insulation	$\mu_{r1} = \mu_{r2} = 1, \epsilon_{r1} = \epsilon_{r2} = 2.7$
Sheath	$\mu_s = 1, \rho_s = 2.84e^{-8} \Omega.m$

Where: ρ_c : Resistivity of the conductor material. ρ_s : Resistivity of the sheath material. μ_c : Relative permeability of the conductor material. μ_s : Relative permeability of the sheath material. μ_r : Relative permeability of the insulating material outside the conductor. ϵ_r : Relative permittivity of the insulating material outside the conductor.

3.4 Load (research nuclear reactor) modeling

A standard component RLCY3 can easily model the load as a Three-Phase Grounded-Wye load with parallel R, L elements $R = 300 \Omega$ and $L = 1.5mH$.

Fig. 3 Fault types



3.5 Asymmetric, symmetric faults modeling

Faults are classified as asymmetric and symmetric faults based on the types shown in Fig. 3 [3, 6]. This type of asymmetrical fault is called a single phase to ground fault (LG), a two-phase fault (LL), and a two-phase fault to ground (LL-G). However, three-phase faults like three-phase short circuit (LLL) and three-phase short circuit to ground (LLL-G) are also symmetric faults. Accordingly, a short circuit is modeled as a time-controlled switch with resistance in ATP/EMTP to study the effects of different fault inception angles and fault resistances.

4 Proposed fault diagnosis technique

Since DFRFT eliminates the discrimination's reliance on signal energy and noise effects and SVD is an efficient feature dimension reduction scheme, our proposed technique makes use of them as a feature extractor and a feature reducer, respectively. Besides, MCSVM is utilized as our classifier because SVM achieves high discrimination efficiency. Among, we used the OVO-SVM to generate all possible paired SVMs with low computational complexity. Additionally, the linear function is chosen as the kernel function to maximize classification performance while minimizing execution time. Figure 4 presents a detailed flowchart for the steps of our proposed fault diagnosis approach, which is divided into three stages. The first stage processes the current signals obtained from the MVC's sending end for various fault types and locations under different conditions. In the second stage, the signals are transformed using DFRFT and SVD to remove the discrimination's dependence on the signal's energy and noise effects. In the third stage, identification, categorization, and tracing are performed using MCSVMs, composed of several binary SVMs. Thus, the most efficient parameters that produce the best results can be identified. The final stage involves the prediction of fault locations using MCSVMs, which are composed of several binary SVMs.

4.1 ATP/EMTP simulated results

Figure 5 shows the simulated design of a practical 22 kV MVC feeding research nuclear reactor. The ATP/EMTP simulation uses a 20 km MVC model, part of the nuclear power plant system published in [31]. Each 1 km in length, twenty identical blocks are connected in a cascade to develop the 20 km MVC model. Faults have been conducted at the intermediate junctions of each consecutive block, and the fault current waveforms are recorded at the sending end only. Faults depend on four main fault parameters: type, distance r , resistance R , and inception angle θ .

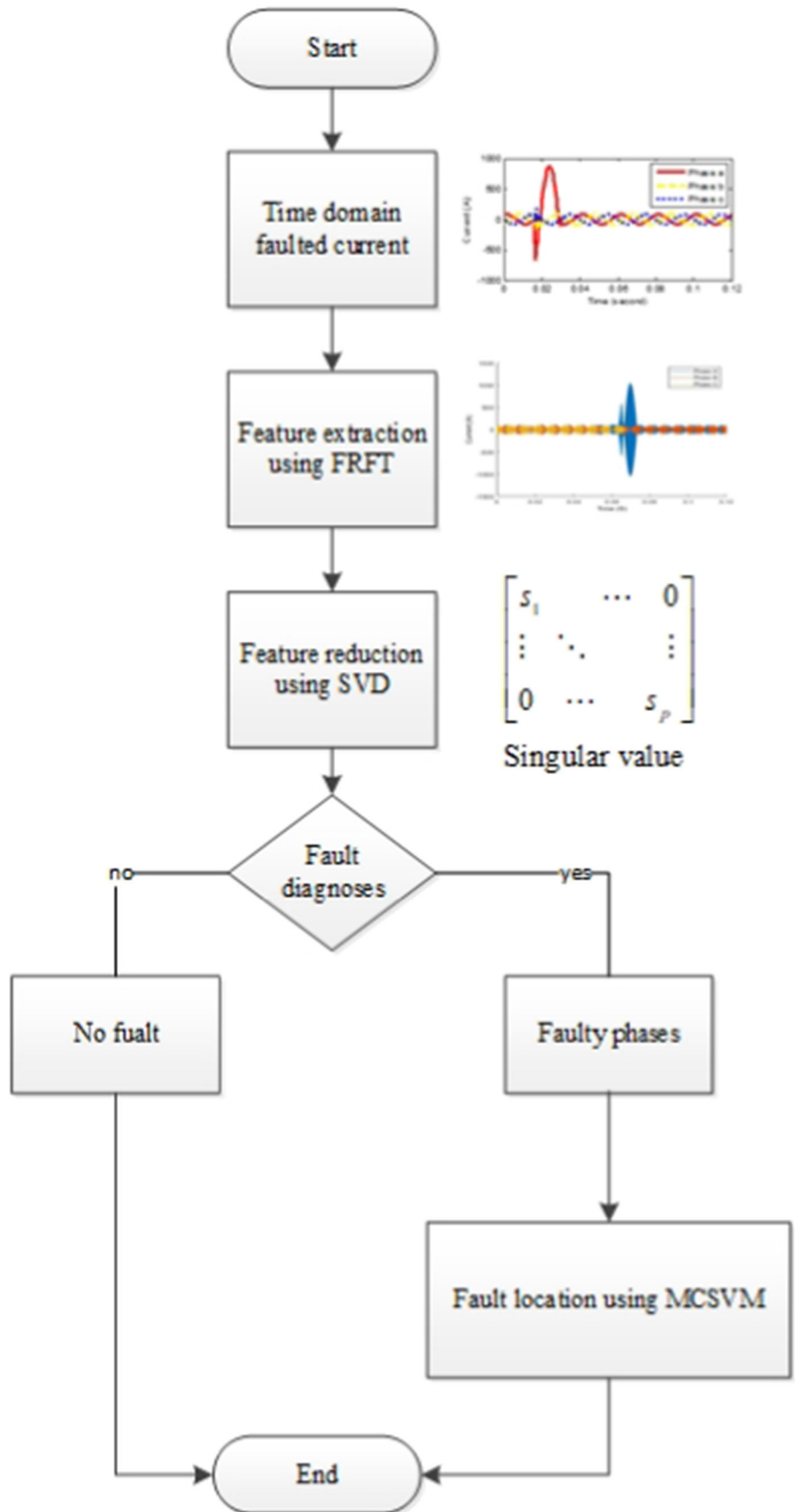
In this regard, five fault types (LG, LL, LL-G, LLL, LLL-G), ten fault resistances in the case of ground fault ($R = 0 \Omega, 10 \Omega, 20 \Omega, 30 \Omega, 40 \Omega, 50 \Omega, 75 \Omega, 100 \Omega, 150 \Omega, 200 \Omega$), five inception angles (including $\theta = 0^\circ, 45^\circ, 90^\circ, 135^\circ, 180^\circ$), and nineteen distances of fault from recording point (including $r = 1 \text{ km}, 2 \text{ km}, 3 \text{ km}, 4 \text{ km}, 5 \text{ km}, 6 \text{ km}, 7 \text{ km}, 8 \text{ km}, 9 \text{ km}, 10 \text{ km}$ (Midpoint), $11 \text{ km}, 12 \text{ km}, 13 \text{ km}, 14 \text{ km}, 15 \text{ km}, 16 \text{ km}, 17 \text{ km}, 18 \text{ km}, 19 \text{ km}$) are simulated. Figure 6 depicts the sending end three-phase current waveforms after applying various fault types to phases at a distance of 10 km (cable midpoint) from the source. These faults are implemented at $\theta = 0^\circ$ for the system phases and $R = 20 \Omega$.

Figure 7 shows the phase (a) current waveform at the sending end under different locations (with fault resistance $R = 20$, inception angle $\theta = 0^\circ$, and fault location $r = (1 \text{ km}, 5 \text{ km}, 10 \text{ km}, 15 \text{ km}, \text{ and } 19 \text{ km})$ for the one-phase (a) to ground fault. The faulted phase current amplitude was reduced from 950A at 1 km to 799A at 19 km by about 16%.

Figure 8 shows the phase (a) current waveform at the sending end under different fault resistances (with fault resistance $R = (10, 20, 50, 75, 100)$, inception angle $\theta = 0^\circ$ and fault location $r = 10 \text{ km}$ for the one-phase (a) to ground fault. It is noticed that the faulted phase current amplitude is reduced at high fault resistance from 1509A at 10Ω to 238A at 100Ω by about 84%.

Figure 9 shows the phase (a) current waveform at the sending end under different inception angles (with fault resistance $R = 20$, inception angle $\theta = (0^\circ, 45^\circ, 90^\circ, 135^\circ, 180^\circ)$ and fault location $r = 10 \text{ km}$ for the one-phase (a) to ground fault.

Fig. 4 Flowchart of the proposed method



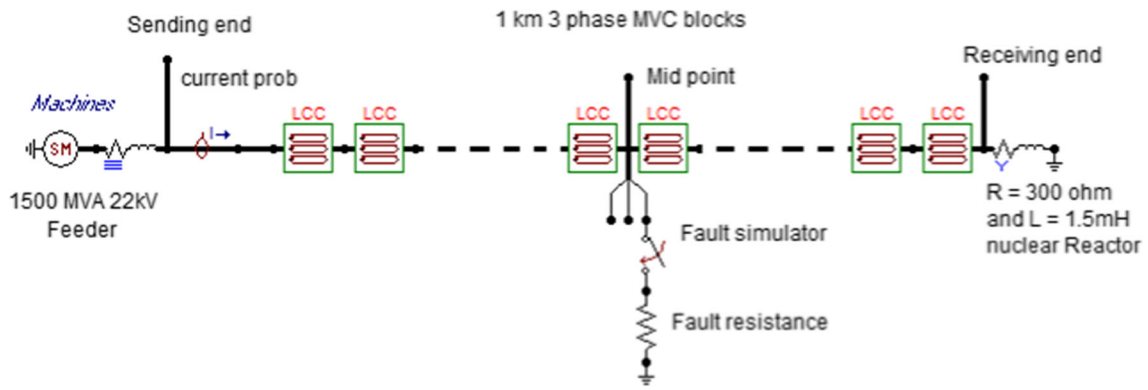


Fig. 5 Simulated MVC model

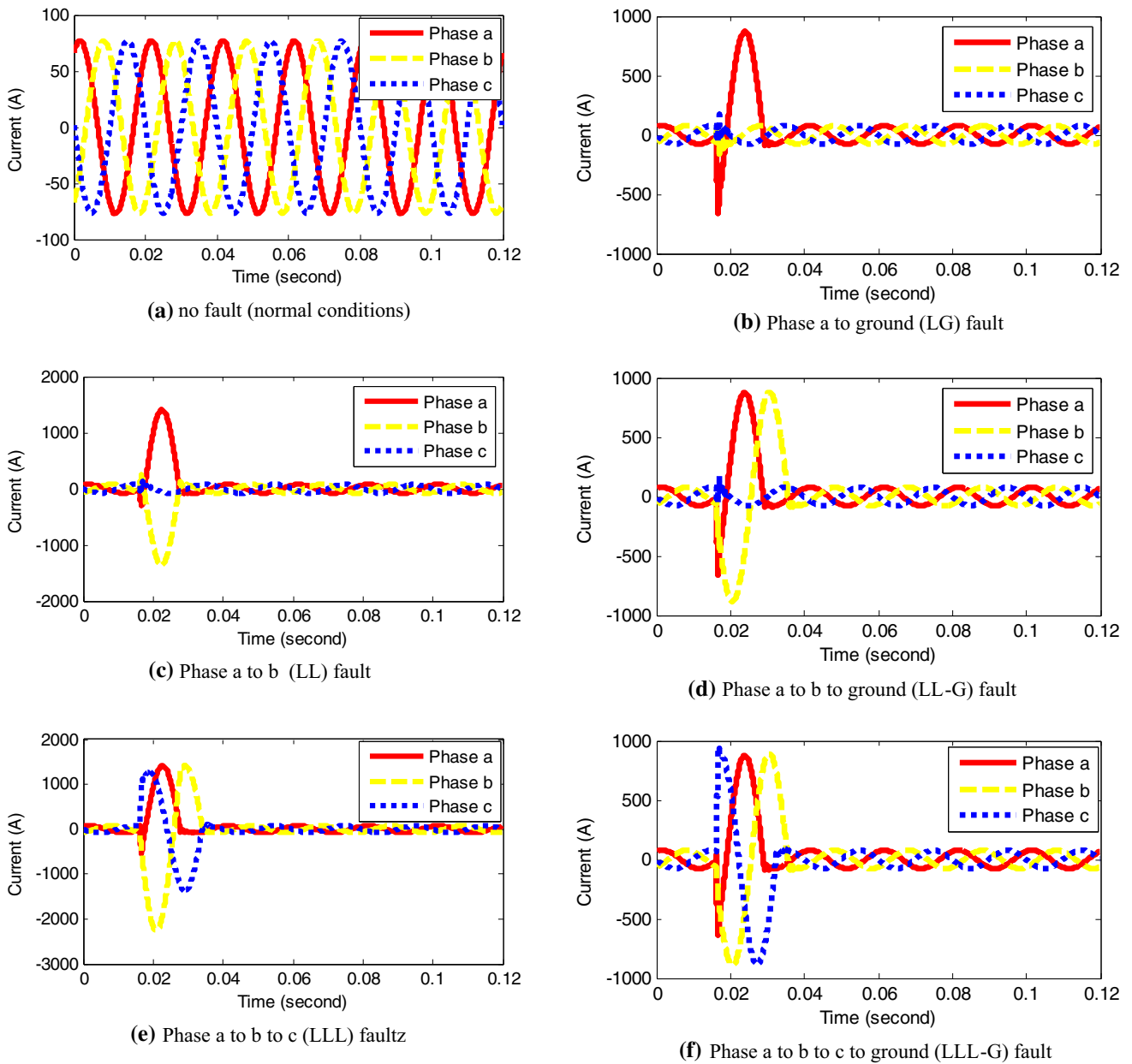


Fig. 6 Three-phase currents waveforms at different faults type (with $R = 20\Omega$, $\theta = 0^\circ$ and $r = 10$ km)

Fig. 7 Phase a current waveform at sending end under different location (with fault resistance $R = 20\Omega$, Inception Angle $\Theta = 0^\circ$ and fault location $r = (1 \text{ km}, 5 \text{ km}, 10 \text{ km}, 15 \text{ km}, 19 \text{ km})$

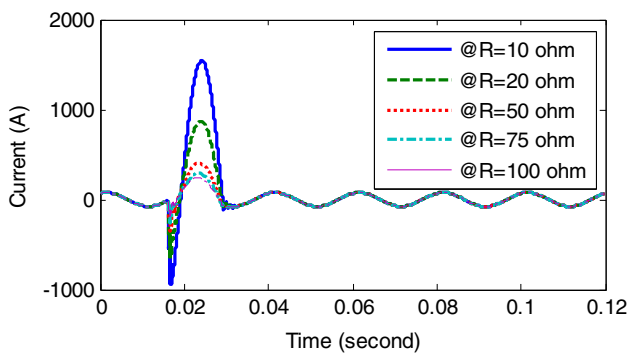
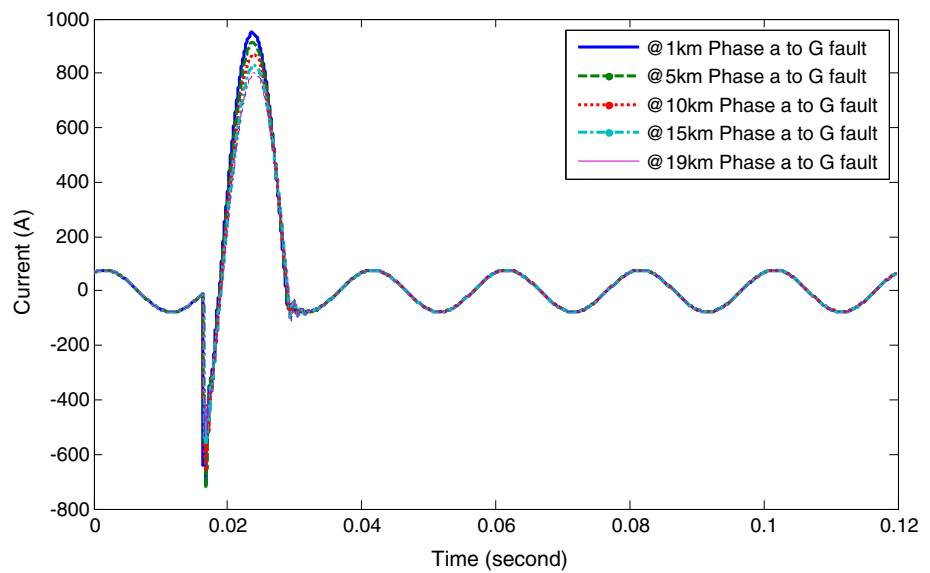


Fig. 8 Phase a current waveform at sending end under different fault resistance (with $R = (10 \Omega, 20 \Omega, 50 \Omega, 75 \Omega, 100\Omega)$, $\Theta = 0^\circ$ and fault location $r = 10 \text{ km}$

It is concluded that the initial current amplitude in the case of fault inception angles of $45^\circ, 90^\circ,$ and 135° is much more than 0° and 180° .

5 Results and discussion

To illustrate the efficiency of the proposed method, five fault types (LG, LL, LL-G, LLL, LLL-G), ten fault resistances in the case of ground fault $R (0 \Omega, 10 \Omega, 20 \Omega, 30 \Omega, 40 \Omega, 50 \Omega, 75 \Omega, 100 \Omega, 150 \Omega, 200 \Omega)$, five inception angles Θ (including $0^\circ, 45^\circ, 90^\circ, 135^\circ, 180^\circ$), and nineteen distances of fault from recording point (including $r = 1 \text{ km}, 2 \text{ km}, 3 \text{ km}, 4 \text{ km}, 5 \text{ km}, 6 \text{ km}, 7 \text{ km}, 8 \text{ km}, 9 \text{ km}, 10 \text{ km}$ (Midpoint), $11 \text{ km}, 12 \text{ km}, 13 \text{ km}, 14 \text{ km}, 15 \text{ km}, 16 \text{ km}, 17 \text{ km}, 18 \text{ km}, 19 \text{ km}$) are simulated. This section describes the related results of Feature extraction, and reduction using DFRFT, SVD fault detection, classification and location via the MCSVM approach.

5.1 Feature extraction, and reduction using DFRFT, SVD

The proposed technique utilizes DFRFT and SVD to extract features. The DFRFT is used because of its fractional power parameter, which allows for a spatial-frequency representation of the signal. As a result, both the spatial and frequency domains can be utilized. By extracting the most significant singular value for each phase, SVD is used to reduce the number of features.

Figure 10 illustrates the output of the DFRFT on various faults' three-phase current signal. This approach eliminates the effect of noise on classification accuracy. In addition, the DFRFT coefficients are used in conjunction with SVD to reduce the number of features, which are then classified using the MCSVM (Fig. 10).

5.2 Fault detection and classification (discrimination) using MCSVM

The main goal is to determine exactly which underground cable is faulty or healthy. To accomplish this, the SVM classifier is fed training current patterns derived from DFRFT and SVD. An SVM will build a hyperplane that separates in an n -dimensional space that forms the boundary between the two data sets if the input data is processed as two pairs of vectors in that space. To compute the margin, we construct two parallel hyperplanes that are superimposed over the two data sets. The hyperplane with the greatest distance to the neighboring data points of both classes, intuitively, gives a suitable separation. The goal is to reduce the classifier's generalization error by increasing the margin or gap between these parallel hyperplanes. The decision function, by utilizing a kernel function, returns the faulty or healthy (No fault).

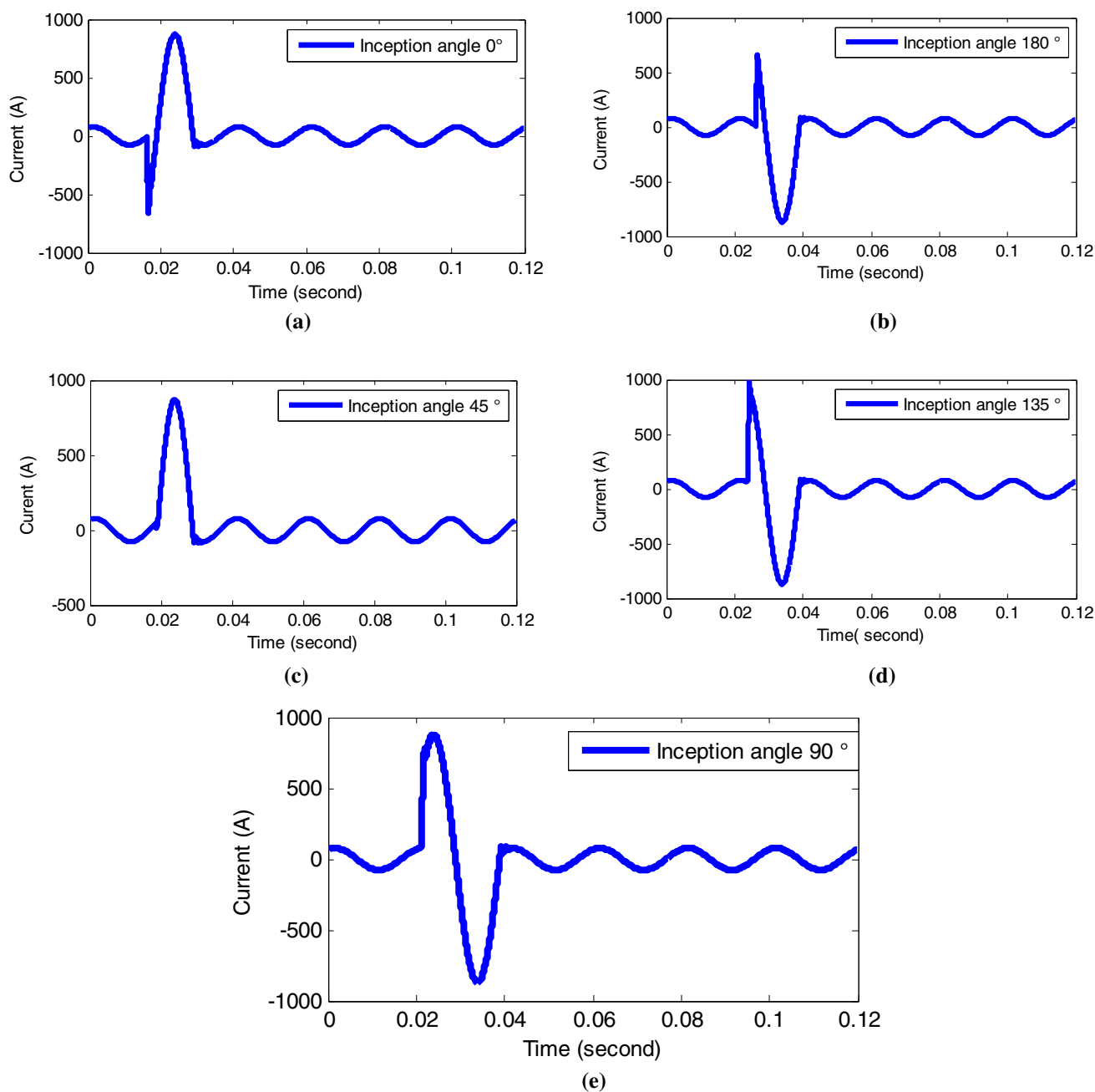
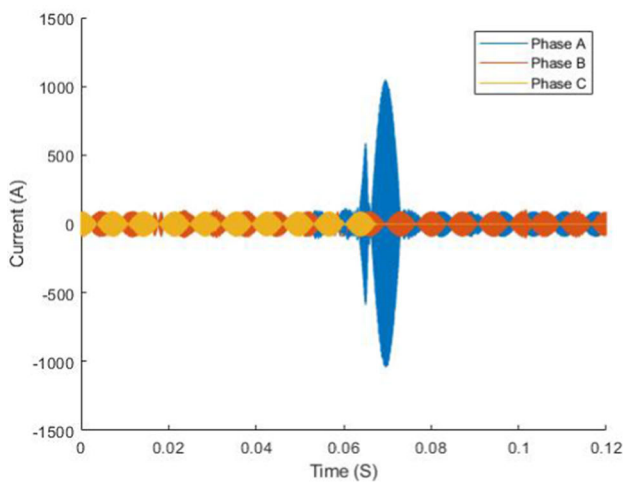


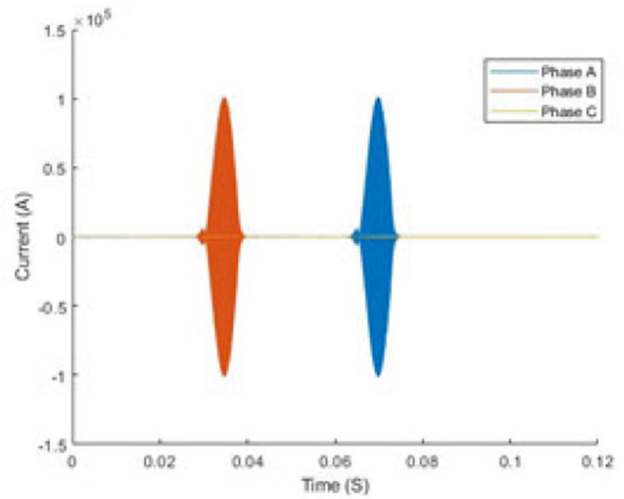
Fig. 9 Phase (a) current waveform at sending end under different inception angle (with fault resistance $R = 20 \Omega$, Inception Angle $\Theta = (0^\circ, 45^\circ, 90^\circ, 135^\circ, 180^\circ)$ and fault location $r = 10$ km

As soon as the faulty phases have been detected, our next goal is to determine the type of fault, at which point the MCSVM is activated. The proposed fault classification approach is divided into two steps. The first is DFRFT feature extraction, followed by SVD reduction, and the second is MCSVM classification. In the first step, the maximum singular value of DFRFT for each fault state is used to produce one feature for each phase. One feature are obtained from the maximum singular value of DFRFT for one phase only. The

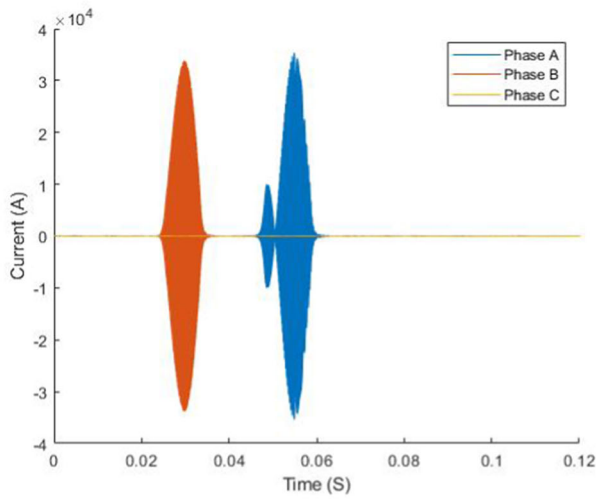
fault currents were gained from ATP/EMTP simulation. The simulation time is 0.12 s with 5 microsecond time step, 10 ms fault clearing. Fault type, fault location and fault inception time are changed to obtain training patterns covering a wide range of different power system conditions. In ATP simulation, the sample frequency is about 120 kHz and the transients of only one-terminal phase currents is processed. For each fault state of a three-phase 22 kV underground cable, three characteristics are retrieved. As a result, the size of the feature



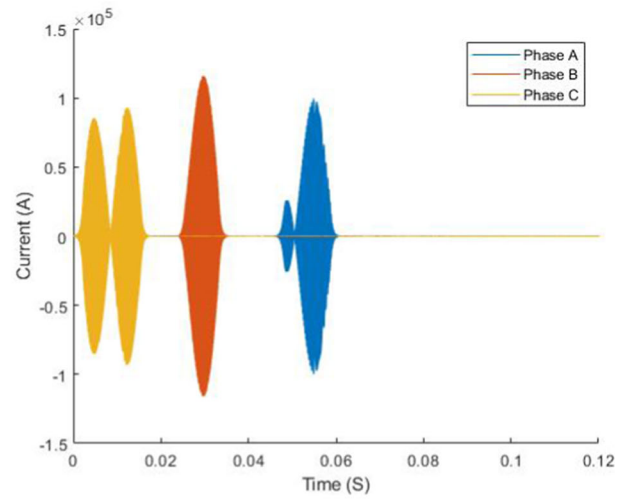
(a) Phase a to ground (LG) fault



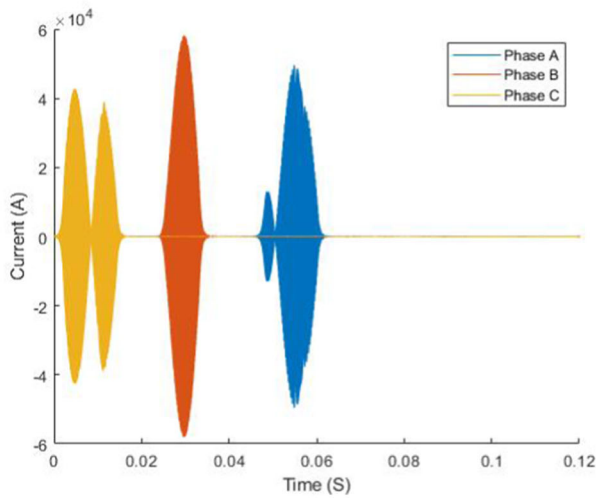
(b) Phase a to b (LL) fault



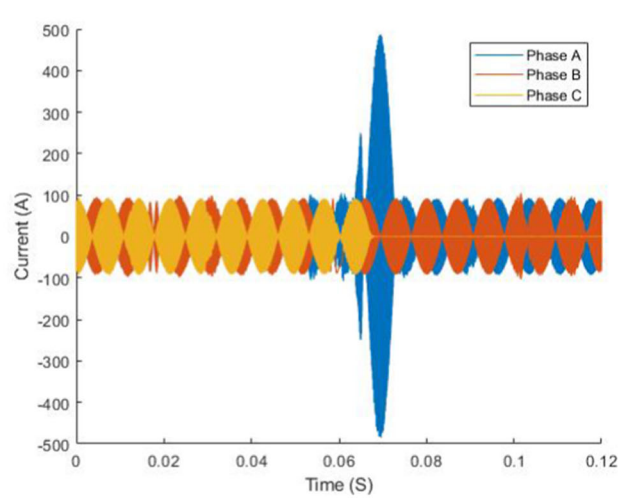
(c) Phase a to b to ground (LL-G) fault



(d) Phase a to b to c (LLL) fault



(e) Phase a to b to c to ground (LLL-G) fault



(f) Phase a to ground (LG) at fault resistance $R=100$ and angle $\Theta=90^\circ$ fault

Fig. 10 The output of DFRFT of different Faults

Table 2 Training label for MCSVM fault type classification

Fault type	Label
No fault	0
LG	1
LL-G	2
LL	3
LLL	4
LLL-G	5

vector, which comprises of three-phase transient characteristics, is 3×950 for each failure type. The MCSVM classifier will be trained and tested using these criteria. We selected the characteristics corresponding to 3×750 faults occurring at 19 distinct locations along the 20 km cable for training. The remaining 3×200 fault cases are used to evaluate the

MCSVM classifier. Table 2 lists the fault types and their associated class labels. The performance and training time using different SVM kernels are shown in figs. 11, 12 and 13. The linear kernel, with the hyperplane discriminating the coefficients properly and the DFRFT fractional factor (α) equal to 0.5, is the most often used kernel.

Linear MCSVM’s performance is compared to that of the k-nearest neighbor method (kNN), probabilistic neural networks (PNN), multilayer perceptron (MLP) and radial basis function networks (RBF). Table 3 presents the fault classification results obtained utilizing various network architectures.

The DFRFT spectrum characteristics for a real signal are conjugated symmetric, which means that the first half of the DFRFT spectrum is a mirrored conjugate to the second half. As a result, the features may be identified using only one half of the DFRFT spectrum, which reduces complexity and saves time. DFRFT and SVD provides optimal representation of

Fig. 11 The proposed method’s performance based on different fractional factor (α) values utilizing Linear, Quadratic, and RBF kernels

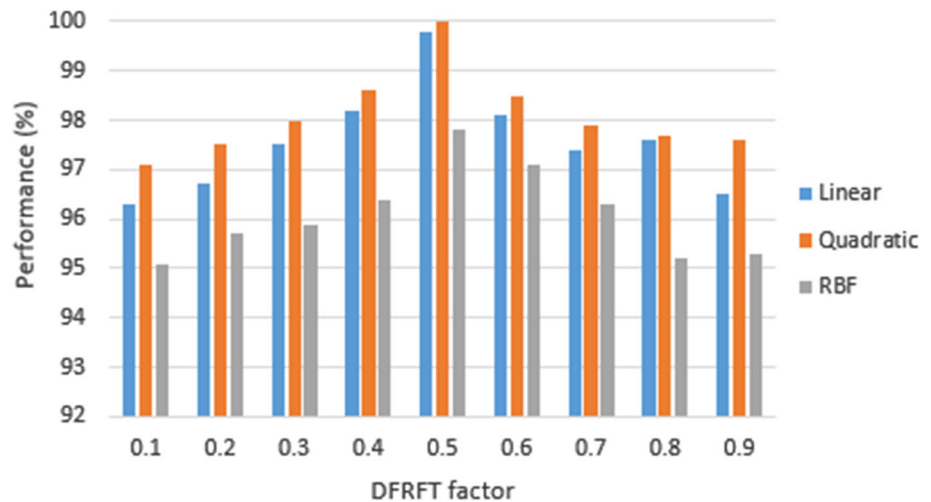


Fig. 12 The proposed method’s execution time is based on fractional factor (α) values utilizing Linear, Quadratic, and RBF kernels

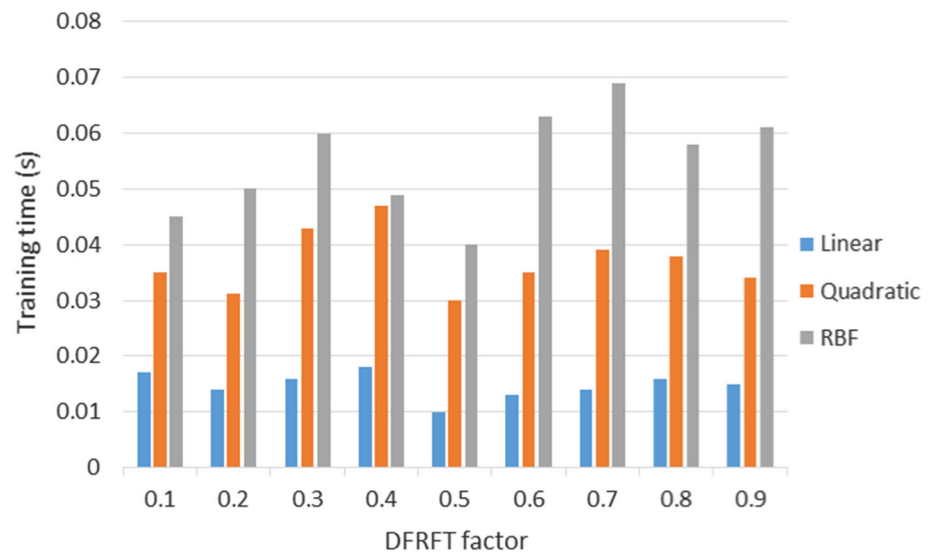


Fig13 The proposed method’s execution time for fractional factor ($\alpha = 0.5$) utilizing Linear, Quadratic, and RBF kernels

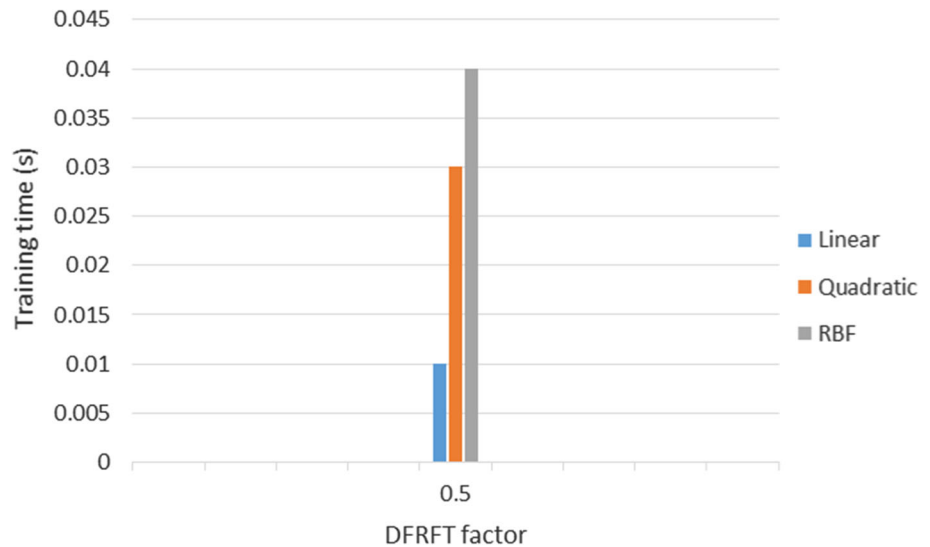


Table 3 Results of several network tests

Classifier	Execution time (s)	Performance (%)
kNN [32]	0.6710	94.14
PNN [33]	0.4121	96.21
MLP [34]	110.283	96.19
RBF [35]	0.3571	95.32
CNN [3]	0.1500	99.60
DFRFT + SVD + MCSVM	0.0100	99.80

signal by packing most of the information in few coefficients for a given signal. The MLP takes a lot of times because the computations are difficult and time consuming and the proper functioning of the model depends on the quality of the training.

As shown in Table 3, the best results were obtained using MCSVM, which achieved 99.8% performance levels and required less execution time than the others since MCSVM is trained using just support vectors rather than the entire training data set. As a result, MCSVM is the optimal option for classification problems. Although the MCSVM has the best classification performance, these results might have happened by chance. To evaluate the MCSVM classifier’s results,

a second validation test is required. Table 4 summarizes the results of the fivefold cross-validation test. The dataset is randomly partitioned into five exclusive subsets of nearly identical size for fivefold cross-validation, and the suggested approach is used five times. Each time, one of the five subsets is used as the test set, while the other four are combined to create the training set. The average percentage error for all five trials is then calculated. In this strategy, it makes no difference how the data is split. Each data point appears exactly once in a test set and four times in a training set. Table 4 shows that all fault categories are appropriately categorized.

5.3 MCSVM-based fault tracking

Our second goal, estimating the fault distance of the underground cable, is triggered after the MCSVM classifier identifies the MVC faulty phases. MCSVM attempts to locate the actual location of the fault using inputs containing three-phase current data. There are several fault types to consider, including single phase-to-ground (LG), phase-to-phase (LL), two-phase-to-ground (LL-G), three-phase (LLL), and three-phase-to-ground (LL-G) (LLL-G). SVM was trained and evaluated using data from simulated faults that occurred at different locations along the 20-km MVC (approximately 19 data points for each case). Furthermore, the resistance and inception angles of faults are changed to illustrate the SVM’s

Table 4 The results of the fivefold cross-validation test

	SVM-1(LG)	SVM-2(LL)	SVM-3(LL-G)	SVM-4(LLL)	SVM-5(LLL-G)
Training	3 × 750	3 × 750	3 × 750	3 × 750	3 × 750
Testing	3 × 200	3 × 200	3 × 200	3 × 200	3 × 200
Performance (%)	100	100	100	100	100

Table 5 Results of SVM-1 for LG faults

Actual location (km)	Estimated location (km)	Error (%)
1	1.0040	0.021053
2	2.0131	0.068947
3	3.0147	0.077368
4	4.0112	0.058947
5	5.0113	0.059474
6	6.0235	0.123684
7	7.0187	0.098421
8	8.0159	0.083631
9	9.0187	0.098526
10	10.0210	0.110579
11	11.0151	0.079526
12	12.0110	0.058421
13	13.0311	0.163684
14	14.0094	0.049474
15	15.0321	0.168947
16	16.0234	0.123158
17	17.0324	0.169158
18	18.0535	0.281579
19	19.0871	0.458474

Table 6 Results of SVM-2 for LL faults

Actual location (km)	Estimated location (km)	Error (%)
1	1.0112	0.058950
2	2.0211	0.111051
3	3.0101	0.053161
4	4.0230	0.121051
5	5.0220	0.115790
6	6.0213	0.112112
7	7.0112	0.058951
8	8.0110	0.057892
9	9.0310	0.163160
10	10.0270	0.142110
11	11.0340	0.178951
12	12.0401	0.104740
13	13.0115	0.060530
14	14.0254	0.133681
15	15.0341	0.179472
16	16.0145	0.076320
17	17.0412	0.216840
18	18.0521	0.274210
19	19.0881	0.463680

performance under varied operating situations. After defining the fault classes, five distinct SVMs (SVM-1–SVM-5) were employed to forecast the locations of LG, LL, LL-G, LLL, and LLL-G problems, respectively. The specific high-frequency features of each type of fault were determined using DFRFT and SVD, and were then employed in the second stage of the method to derive the revised location of the fault.

The results demonstrate that the cable's nearest points have the highest estimate errors. In terms of fault localization accuracy, similar findings have been found for various fault kinds and system situations. After defining the fault classes, five distinct SVMs (SVM-1–SVM-5) were used to forecast the locations of LG, LL, LL-G, and LLL-G problems. Tables 5, 6, 7, 8 and 9 provide the SVM-1–SVM-5 testing results. In the worst-case situation, the maximum percentage inaccuracy in identifying the fault is restricted to (0.47% of total line length) kilometers, as indicated in the tables. Each test case's SVM results were examined to determine the estimation error associated with that test instance. The difference between the estimated fault distance (A) and the actual fault distance (r) for the test instance was used to quantify the inaccuracy. The accuracy of the method is equal to this estimation error. The algorithm's accuracy decreases as the distance deviation increases. The overall accuracy, E , is defined as the highest estimate error for the line's whole length range,

Table 7 Results of SVM-3 for LL-G faults

Actual location (km)	Estimated location (km)	Error (%)
1	1.0011	0.005789
2	2.0123	0.064737
3	3.0213	0.112105
4	4.0030	0.015789
5	5.0313	0.164737
6	6.0543	0.285789
7	7.0453	0.238421
8	7.9840	0.084210
9	9.0083	0.043684
10	10.0013	0.006842
11	11.0713	0.375263
12	12.0210	0.110526
13	13.0100	0.052632
14	14.0153	0.080526
15	14.9984	0.008420
16	16.0311	0.163684
17	17.0513	0.270000
18	18.0793	0.417368
19	19.0899	0.473316

Table 8 Results of SVM-4 for LLL faults

Actual location (km)	Estimated location (km)	Error (%)
1	1.0005	0.002632
2	2.0103	0.054211
3	2.9983	0.008947
4	4.0000	0.000000
5	5.0017	0.008947
6	6.0041	0.021579
7	7.0453	0.238421
8	7.9990	0.005263
9	9.0782	0.411579
10	10.0101	0.053158
11	11.0610	0.321053
12	12.0220	0.115789
13	13.0010	0.005263
14	14.0114	0.060000
15	15.0010	0.005263
16	16.0451	0.237368
17	16.9198	0.422105
18	18.0893	0.470000
19	19.0910	0.478947

Table 9 Results of SVM-5 for LLL-G faults

Actual location (km)	Estimated location (km)	Error (%)
1	1.0210	0.110526
2	2.0125	0.065789
3	3.0351	0.184737
4	4.0148	0.077895
5	5.0320	0.168421
6	6.0112	0.058947
7	7.0010	0.005263
8	8.0090	0.0473684
9	9.0159	0.083684
10	10.0311	0.163684
11	11.0195	0.102632
12	12.0125	0.065789
13	13.0209	0.110000
14	14.0311	0.163684
15	15.0171	0.090000
16	16.0412	0.216842
17	17.0491	0.258421
18	18.0537	0.282632
19	19.0897	0.472105

as well as for all conceivable fault types, expressed as a percentage of the total line length L .

$$\text{Error}(E) = \left| \frac{\text{estimated location } (A) - \text{exact location } (r)}{\text{total cable length } (L)} \right| \times 100 \tag{12}$$

Table 10 shows the actual and estimated locations of faults at 19 kms with various fault resistance and inception angles. The location of the fault, the resistance of the fault, and the angle of inception all affect the accuracy of fault location. The maximum error (0.525789) in fault location occur when the fault resistance is equal to 200 Ω and the inception angle is 90 degrees at the cable receiving end (19 km), as shown in Table 10.

The results of this research demonstrate that using MCSVM in conjunction with DFRFT and SVD is an excellent strategy for identifying faults on subterranean cable feeding research nuclear reactor. The suggested approach may conveniently, rapidly, and precisely locate the position of the fault.

6 Conclusion

This paper presented a novel fault classification technique and location in a MVC research nuclear reactor that uses MCSVM. First, ATP/EMTP simulates several faults with varying fault locations under varying conditions to prepare input data. Additionally, optimize classification and localization performance and execution time by combining DFRFT with SVD and MCSVM. The influence of the rotation angle of the DFRFT on classification efficiency was also investigated, and it was observed that classification efficiency varies with the rotation angle value. SVM linear, quadratic, and RBF kernels were used for classification. The results indicate that a quadratic kernel is the most efficient due to the quadratic plane’s efficient separation of classes. The most obvious conclusion from examining various DFRFT factors is that 0.5 factors perform the best in linear and quadratic kernels.

On the other hand, the complexity of the kernel is the critical determinant of execution time. Thus, the linear kernel executes at the fastest rate, attaining 99.8% performance and a time of 0.01 s for various faults at multiple locations, resistances, and angles of inception. The maximum error is equal to 0.525789% in fault location occur the fault resistance is equivalent to 200 Ω and the inception angle is 90⁰ at the MVC receiving end. This shows that the proposed technique can offer acceptable accuracy in fault classification and fault location estimation. Moreover, MCSVM could be used as a part of a new generation of high-speed advanced fault locators.

Table 10 Testing results of MCSVM for different fault resistances and inception angle

R (Ω)	Fault types	Inception angle Θ										
		0^0			45^0		90^0		135^0		180^0	
		X(km)	Y(km)	E (%)	Y(km)	E (%)	Y(km)	E (%)	Y(km)	E (%)	Y(km)	E (%)
10 Ω	LG	19	19.0981	0.516315	19.0823	0.433158	19.0990	0.521053	19.0872	0.458947	19.0982	0.516842
	LL	19	19.0881	0.463684	19.0891	0.468947	19.0981	0.516316	19.0881	0.463684	19.0883	0.464737
	LLG	19	19.0798	0.420000	19.0923	0.485789	19.0898	0.472632	19.0918	0.483158	19.0798	0.42
	LLL	19	19.0788	0.414737	19.0844	0.444211	19.0988	0.520000	19.0888	0.467368	19.0787	0.414211
	LLL _G	19	19.0815	0.428947	19.0913	0.480526	19.0999	0.525789	19.0905	0.476316	19.0815	0.428947
20 Ω	LG	19	19.0973	0.512105	19.0888	0.467368	19.0933	0.491053	19.0887	0.466842	19.0972	0.511579
	LL	19	19.0866	0.455789	19.0844	0.444211	19.0917	0.482632	19.0855	0.450000	19.0866	0.455789
	LLG	19	19.0812	0.427368	19.0977	0.514211	19.0982	0.516842	19.0987	0.519474	19.0833	0.438421
	LLL	19	19.0798	0.420000	19.0901	0.474211	19.0971	0.511053	19.0921	0.484737	19.0796	0.418947
	LLL _G	19	19.0956	0.503158	19.0923	0.485789	19.0994	0.523158	19.0941	0.495263	19.0854	0.449474
30 Ω	LG	19	19.0967	0.508947	19.0823	0.433158	19.0991	0.521579	19.0825	0.434211	19.0965	0.507895
	LL	19	19.0877	0.461579	19.0891	0.468947	19.0988	0.520000	19.0894	0.470526	19.0873	0.459474
	LLG	19	19.0945	0.497368	19.0923	0.485789	19.0911	0.479474	19.0923	0.485789	19.0943	0.496316
	LLL	19	19.0777	0.408947	19.0844	0.444211	19.0984	0.517895	19.0842	0.443158	19.0776	0.408421
	LLL _G	19	19.0988	0.520000	19.0923	0.485789	19.0958	0.504211	19.0921	0.484737	19.0985	0.518421
40 Ω	LG	19	19.0987	0.519474	19.0876	0.461053	19.0975	0.513158	19.0878	0.462105	19.0988	0.520000
	LL	19	19.0865	0.455263	19.0834	0.438947	19.0978	0.514737	19.0837	0.440526	19.0864	0.454737
	LLG	19	19.0872	0.458947	19.0969	0.510000	19.0987	0.519474	19.0968	0.509474	19.0871	0.458421
	LLL	19	19.0799	0.420526	19.0911	0.479474	19.0978	0.514737	19.0913	0.480526	19.0798	0.420000
	LLL _G	19	19.0944	0.496842	19.0933	0.491053	19.0989	0.520526	19.0932	0.490526	19.0945	0.497368
50 Ω	LG	19	19.0959	0.504737	19.0825	0.434211	19.0996	0.524211	19.0824	0.433684	19.0957	0.503684
	LL	19	19.0866	0.455789	19.0899	0.473158	19.0988	0.520000	19.0898	0.472632	19.0867	0.456316
	LLG	19	19.0812	0.427368	19.0935	0.492105	19.0936	0.492632	19.0936	0.492632	19.0813	0.427895
	LLL	19	19.0798	0.420000	19.0839	0.441579	19.0951	0.500526	19.0836	0.440000	19.0797	0.419474
	LLL _G	19	19.0856	0.450526	19.0945	0.497368	19.0979	0.515263	19.0942	0.495789	19.0855	0.450000
60 Ω	LG	19	19.0973	0.512105	19.0894	0.470526	19.0996	0.524211	19.0898	0.472632	19.0970	0.510526
	LL	19	19.0866	0.455789	19.0870	0.457895	19.0984	0.517895	19.0874	0.460000	19.0865	0.455263
	LLG	19	19.0812	0.427368	19.0982	0.516842	19.0992	0.522105	19.0985	0.518421	19.0811	0.426842
	LLL	19	19.0798	0.420000	19.0939	0.494211	19.0981	0.516316	19.0936	0.492632	19.0789	0.415263
	LLL _G	19	19.0922	0.485263	19.0987	0.519474	19.0958	0.504211	19.0988	0.520000	19.0935	0.492105
75 Ω	LG	19	19.0911	0.479474	19.0877	0.461579	19.0991	0.521579	19.0873	0.459474	19.0910	0.478947
	LL	19	19.0920	0.484211	19.0916	0.482105	19.0914	0.481053	19.0914	0.481053	19.0922	0.485263
	LLG	19	19.0915	0.481579	19.0904	0.475789	19.0934	0.491579	19.0905	0.476316	19.0916	0.482105
	LLL	19	19.0959	0.504737	19.0918	0.483158	19.0989	0.520526	19.0919	0.483684	19.0954	0.502105
	LLL _G	19	19.0934	0.491579	19.0934	0.491579	19.0965	0.507895	19.0933	0.491053	19.0937	0.493158
100 Ω	LG	19	19.0949	0.499474	19.0913	0.480526	19.0988	0.520000	19.0915	0.481579	19.0948	0.498947
	LL	19	19.0989	0.520526	19.0922	0.485263	19.0939	0.494211	19.0927	0.487895	19.0986	0.518947
	LLG	19	19.0998	0.525263	19.0936	0.492632	19.0969	0.510000	19.0935	0.492105	19.0996	0.524211
	LLL	19	19.0985	0.518421	19.0916	0.482105	19.0988	0.520000	19.0918	0.483158	19.0984	0.517895

Table 10 (continued)

R (Ω)	Fault types	Inception angle Θ										
		0^0			45^0		90^0		135^0		180^0	
		X(km)	Y(km)	E (%)	Y(km)	E (%)	Y(km)	E (%)	Y(km)	E (%)	Y(km)	E (%)
150 Ω	LLG	19	19.0999	0.525789	19.0933	0.491053	19.0977	0.514211	19.0936	0.492632	19.0998	0.525263
	LG	19	19.0919	0.483684	19.0932	0.490526	19.0988	0.520000	19.0936	0.492632	19.0929	0.488947
	LL	19	19.0978	0.514737	19.0954	0.502105	19.0988	0.520000	19.0954	0.502105	19.0977	0.514211
	LLG	19	19.0987	0.519474	19.0984	0.517895	19.0977	0.514211	19.0988	0.520000	19.0986	0.518947
	LLL	19	19.0976	0.513684	19.0949	0.499474	19.0941	0.495263	19.0947	0.498421	19.0979	0.515263
200 Ω	LLL	19	19.0989	0.520526	19.0977	0.514211	19.0977	0.514211	19.0979	0.515263	19.0987	0.519474
	LG	19	19.0941	0.495263	19.0912	0.480000	19.0967	0.508947	19.0922	0.485263	19.0944	0.496842
	LL	19	19.0981	0.516316	19.0932	0.490526	19.0938	0.493684	19.0943	0.496316	19.0983	0.517368
	LLG	19	19.0998	0.525263	19.0918	0.483158	19.0905	0.476316	19.0919	0.483684	19.0994	0.523158
	LLL	19	19.0976	0.513684	19.0988	0.520000	19.0915	0.481579	19.0987	0.519474	19.0979	0.515263
	LLL	19	19.0999	0.525789	19.0985	0.518421	19.0999	0.525789	19.0989	0.520526	19.0998	0.525263

Funding Open access funding provided by The Science, Technology & Innovation Funding Authority (STDF) in cooperation with The Egyptian Knowledge Bank (EKB).

Open Access This article is licensed under a Creative Commons Attribution 4.0 International License, which permits use, sharing, adaptation, distribution and reproduction in any medium or format, as long as you give appropriate credit to the original author(s) and the source, provide a link to the Creative Commons licence, and indicate if changes were made. The images or other third party material in this article are included in the article's Creative Commons licence, unless indicated otherwise in a credit line to the material. If material is not included in the article's Creative Commons licence and your intended use is not permitted by statutory regulation or exceeds the permitted use, you will need to obtain permission directly from the copyright holder. To view a copy of this licence, visit <http://creativecommons.org/licenses/by/4.0/>.

References

- Ohki, Yoshimichi, and Naoshi Hirai (2016) Fault location in a cable for a nuclear power plant by frequency domain reflectometry. In: 2016 International Conference on Condition Monitoring and Diagnosis (CMD). IEEE, 2016
- Lim H, Kwon G-Y, Shin Y-J (2021) Fault detection and localization of shielded cable via optimal detection of time–frequency-domain reflectometry. *IEEE Trans Instrum Meas* 70:1–10
- Said A et al (2022) Deep learning-based fault classification and location for underground power cable of nuclear facilities. *IEEE Access* 10:70126–70142
- Chu SC (1969) Screening factor of pipe-type cable systems. *IEEE Trans Power App Syst* 88(5):522–528
- Nowlen, Steven P (2004) *Cable Failure Modes and Effects Risk Analysis Perspectives*. Probabilistic Safety Assessment and Management. Springer, London
- Dashti R et al (2021) A survey of fault prediction and location methods in electrical energy distribution networks. *Measurement* 184:109947
- Shadi, Mohammad Reza, et al. "A Parameter-Free Approach for Fault Section Detection on Distribution Networks Employing Gated Recurrent Unit." *Energies* 14.19 (2021): 6361.
- Ghoniem AS (2019) Sub-Line Transient Magnetic Fields Calculation Approach for Fault detection, classification and location of High Voltage Transmission Line. *International Journal on Electrical Engineering and Informatics* 11(3):548–563
- Fahim SR, Sarker SK, Muyeen SM, Sheikh MRI, Das SK (2020) Microgrid fault detection and classification: Machine learning based approach, comparison, and reviews. *Energies* 13:3460
- Mirshakali, H.; Dashti, R.; Shaker, H.R. An Accurate Fault Location Algorithm for Smart Electrical Distribution Systems Equipped with Micro Phasor Measurement Units. In *Proceedings of the 2019 International Symposium on Advanced Electrical and Communication Technologies, ISAECT 2019, Rome, Italy, 27–29 November 2019*.
- Shi Y, Zheng T, Yang C (2020) Reflected traveling wave based single-ended fault location in distribution networks. *Energies* 13:3917
- Liu Y, Sakis Meliopoulos AP, Tan Z, Sun L, Fan R (2017) Dynamic state estimation-based fault locating on transmission lines. *IET-Gen Trans Dist* 11:4184–4192
- Bayati N, Mortensen LK, Savaghebi M, Shaker HR (2022) A localized transient-based fault location scheme for distribution systems. *Sensors* 22:2723
- Bayati N, Baghaee HR, Hajizadeh A, Soltani M, Lin Z, Savaghebi M (2021) Local fault location in meshed dc microgrids based on parameter estimation technique. *IEEE Syst J* 16:1606–1615
- Bayati N, Balouji E, Baghaee HR, Hajizadeh A, Soltani M, Lin Z, Savaghebi M (2021) Locating high-impedance faults in dc microgrid clusters using support vector machines. *Appl Energy* 308:118338
- Chen K, Hu J, Zhang Y, Yu Z, He J (2019) Fault location in power distribution systems via deep graph convolutional networks. *IEEE J Sel Areas Commun* 38:119–131
- Usman MU, Faruque O (2018) Validation of a PMU-based fault location identification method for smart distribution network with

- photovoltaics using real time data. *IET Gener Transm Distrib* 12:5824–5833
18. Cavalcante PA, de Almeida MC (2018) Fault location approach for distribution systems based on modern monitoring infrastructure. *IET Gener Transm Distrib* 12:94–103
 19. Salim RH, Salim KCO, Bretas AS (2011) Further improvements on impedance-based fault location for power distribution systems. *IET Gener Transm Distrib* 5:467–478
 20. Lovisolo L, Neto JM, Figueiredo K, de Menezes Laporte L, dos Santos Rocha JC (2012) Location of faults generating short-duration voltage variations in distribution systems regions from records captured at one point and decomposed into damped sinusoids. *IET Gener Transm Distrib* 6:1225–1234
 21. Shi X, Xu Y (2021) A fault location method for distribution system based on one-dimensional convolutional neural network. In: Proceedings of the 2021 IEEE International Conference on Power, Intelligent Computing and Systems (ICPICS), Shenyang, China, 29–31 July 2021; pp. 333–337.
 22. Shi S, Zhu B, Lei A, Dong X (2019) Fault location for radial distribution network via topology and reclosure-generating traveling waves. *IEEE Trans Smart Grid* 10:6404–6413
 23. Cole, Ronald, et al. "Bus Differential Protection Upgrade for a 1,500 MVA Nuclear Power Plant With Atypical Connections"
 24. Ozaktas H, Arikan O, Kutay M, Bozdogan G (1996) Digital computation of the fractional Fourier transform. *IEEE Trans Signal Process* 44:2141
 25. Krishna BT (2012) Fractional Fourier transform, In: proceedings of the International Conference on Advances in Computing, Communications and Informatics (ICACCI'12), Chennai, India, 3–5 August 2012, ACM Press
 26. Awad M, Khanna R (2015) Efficient learning machines. Theories, concepts, and applications for engineers and system designers, Apress, Berkeley USA
 27. Tong S, Koller D (2002) Support vector machine active learning with applications to text classification. *J Mach Learn Res* 2:45
 28. van den Burg G, Groenen P (2016) GenSVM: A generalized multiclass support vector machine. *J Mach Learn Res* 17:1–42
 29. Said A (2018) Analysis of 500 kV OHTL polluted insulator string behavior during lightning strokes. *Int J Electr Power Energy Syst* 95:405–416
 30. Eldin EMT et al (2006) An accurate fault location scheme for connected aged cable lines in double-fed systems. *Electr Eng* 88(5):431–439
 31. Wang Li et al (2019) A speed-governing system model with over-frequency protection for nuclear power generating units. *Energies* 13(1):1–1
 32. Asadi Majd A, Samet H, Ghanbari T (2017) k-NN based fault detection and classification methods for power transmission systems. *Prot Control Mod Power Syst* 2:32
 33. Ngaopitakkul, Athapol, and Nuchitita Suttisinthong. "Discrete wavelet transform and probabilistic neural network algorithm for classification of fault type in underground cable." In: 2012 International Conference on Machine Learning and Cybernetics. Vol. 1. IEEE, 2012.
 34. Eboule Pouabe PS, Ali N. Hasan, and Bhekisipho Twala. "The use of multilayer perceptron to classify and locate power transmission line faults." *Artificial Intelligence and Evolutionary Computations in Engineering Systems*. Springer, Singapore, 2018. 51–58
 35. Lin W-M et al (2001) A fault classification method by RBF neural network with OLS learning procedure. *IEEE Power Energy Mag* 21:60–60

Publisher's Note Springer Nature remains neutral with regard to jurisdictional claims in published maps and institutional affiliations.